



Partial substitution of cement by the association of Ferronickel slags and *Crepidula fornicata* shells

Manal Bouasria^a, Fouzia Khadraoui^a, Mohammed-Hichem Benzaama^a, Karim Touati^a, Daniel Chateigner^b, Stéphanie Gascoin^b, Valérie Pralong^b, Beate Orberger^c, Laidi Babouri^d, Yassine El Mendili^{a,*}

^a COMUE Normandie Université – Laboratoire ESITC, 1 Rue Pierre et Marie Curie, 14610, Epron, France

^b CRISMAT-ENSICAEN, UMR CNRS 6508, Université de Caen Normandie, IUT Caen, Normandie Université, 6 Boulevard Maréchal Juin, 14050, Caen, France

^c GEOPS, Université Paris-Sud, UMR 8148 (CNRS-UPS), Bât. 504, 91405, Orsay, France

^d École Normale Supérieure d'Enseignement Technologique de Skikda, Université du 20, Août 1955, Skikda, Algeria

ARTICLE INFO

Keywords:

Ferronickel slag
Crepidula shells
 microstructural Characterization
 Mechanical properties
 Waste valorization

ABSTRACT

Environmental impacts of building materials can be achieved by reducing the amount of cement in cementitious composites, specifically when incorporating wastes as partial replacement of Portland cement. In this work we substitute cement by shell by-products and Ferronickel Slags (FNS) while keeping interesting specific properties. FNS associated to *Crepidula fornicata* shells (CR) are good candidates to replace part of the Portland cement as they have appropriate physicochemical properties, and are available at high abundance.

The effect of the association of FNS and CR on the mechanical properties of mortar is investigated. Microstructural characterization of these additives are carried out using Scanning Electron Microscopy, X-Ray diffraction and Raman spectroscopy. Formulated mortars contain different mixes of FNS-CR and Portland cement. Specific surface area, workability and setting times of fresh mortars are studied. The mechanical properties are investigated using 3-point bending and compressive tests for curing periods ranging from 2 to 28 days. In the fresh state, the replacement of cement by up to 20 wt.% of FNS-CR does not significantly affect mortar properties. However, at the hardened state, the setting time is increased using FNS-CR. With up to 20% wt.% of FNS-CR incorporation, the mechanical properties are similar or even slightly larger than that of the control mortar.

1. Introduction

Cement manufacturing contributes significantly to CO₂ emissions [1], as it is the most widely used substance in the world [2]. About 4.65 billion tons are necessary each year worldwide for the construction material sector, generating around 4 billion tons of CO₂ [3]. This contributes as much as 7% to the total anthropogenic footprint [4]. The enhanced use of additives in the cement manufacturing will significantly reduce the CO₂ footprint. Therefore, the search for new supplementary cementitious materials (SCM) has become a greater concern for the manufacture of cements. The use of waste including industrial by-products as cement substitution presents a promising solution [5]. One of these products is slag, a waste available from ferro-nickel production through pyrometallurgical processing [6–10].

The Société Le Nickel (SLN, New Caledonia) has been continuously

producing nickel from laterites over 145 years [11,12]. SLN produces annually about 3 million tons of FNS with an existing stockpile of 25 million tons [13]. At present, only 8% of the annual FNS production is used [8]. The rest of the FNS is stockpiled on site at high storage costs to prevent environmental impact [14,15]. These slags provide a valuable resource for being recycled.

The FNS from SLN are free of harmful substances and present excellent properties such as high density, sufficient hardness and toughness, good compaction potential, high water permeability and high fire resistance with low thermal expansion [13]. Therefore this material can be used as construction materials [13]. The recycling of slags in the building industry has an additional value to the cement properties [16]. SLN therefore transforms FNS into an economic resource. The commercial product “SLAND” is exported to Australia being used as SCM [13], or FNS is used as base filler for road

* Corresponding author.

E-mail address: yassine.el-mendili@esitc-caen.fr (Y. El Mendili).

<https://doi.org/10.1016/j.jobe.2020.101587>

Received 31 March 2020; Received in revised form 13 June 2020; Accepted 15 June 2020

Available online 18 June 2020

2352-7102/© 2020 Elsevier Ltd. All rights reserved.

construction [19]. However, the FNS can be used also as cement additives, if their physicochemical characteristics are appropriate [17,18].

Another potential waste material abundant in nature which can play the role of SCM are mollusc shells, among which farmed seashells represent the largest available volumes. For example, in France, among the biggest consumer of shellfish in Europe, oyster and mussel farming generates large amounts of shell wastes, available for reusability. Included in such wastes are also present shells from inedible invasive species like *Crepidula fornicata*. All in all, annually, nearly 200000 tons of shells end up for their major part in landfills for amendments in Ca, incinerators or as litter in the environment in France [21]. This is cost intensive and contains some environmental drawbacks.

Historically, seashells have been used in concrete for specific type of building material called 'Tabby' during the late 1700s. Tabby is a type of concrete made by burning oyster shells to create lime before mixing with sand, ash, broken oyster shells as aggregate and water. Tabby was used by early Spanish explorers in North Carolina and Florida in the 16th century, then by British colonists primarily in South Carolina and Georgia around 1700 [22]. The studies on the use of seashell as SCM have been going on for 50 years [23,24], showing that ground seashells can be applied in mortars. Mortars with partial replacement of cement by seashells can present an adequate strength and lower thermal conductivity compared to usual mortars. The seashells are composed of at least 95 wt.% of calcium carbonate (CaCO_3), a bit less than the calcium carbonate contents of limestone powders used for Portland cement production [25].

The main composition of *Crepidula* shells is calcium carbonate (CaCO_3), which can be used as supplementary cementitious material. According to the European standard EN 197-1 [26], calcium carbonate (CaCO_3) or limestone can be added up to 35% in Portland cement. CaCO_3 acts mainly as an inert filler when the replacement level is larger than 5% due to its low solubility. The inert property and less reactivity of carbonate limits its use in cement industry [27]. The use of slag in blended cement can improve the later age strength but results in lower early age strength due to the need of activation and its slow hydration. Efforts have been made to use carbonate in ternary blended cements to improve the strength at the early age. Different studies show that the combination of calcium carbonate (as limestone) and slag in concrete or mortar is complementary. Indeed, the calcium carbonate filler will improve the early strength of concrete while slags will improve later strengths and thus achieve an optimal strength development [28,29].

In this study, we focus on the use of *Crepidula fornicata* shells (CR) and FNS as a structural component with a partial replacement in mortar. For that purpose, an experimental study of the soundness and compressive strength of specimens made with this mixture is carried out. Different mortar mixtures using different percentages of slags and CR shells are cast and tested up to failure.

2. Materials and methods

2.1. Materials and samples preparation

2.1.1. Cement

The cement used in this study is a CEM I 52.5 N made by the French company Calcia according to the EN 197-1 standard [26]. The Blaine fineness is $4100 \text{ cm}^2 \text{ g}^{-1}$, and the density is 3.2 g cm^{-3} . The clinker ratio is 95% and the cement mineralogical composition is: $\text{C}_3\text{S} = 74\%$, $\text{C}_2\text{S} = 12\%$, $\text{C}_3\text{A} = 11\%$, $\text{SO}_3 = 2.7\%$, $\text{S}^{2-} < 0.02\%$ and $\text{Na}_2\text{O} = 0.06\%$. The chemical composition is given in Table 1.

Table 1

Chemical composition of CEM I 52.5 N cement in wt.%. a) obtained by Energy Dispersive X-Ray spectroscopy and b) obtained by X-ray fluorescence (XRF).

Component	SiO ₂	CaO	Al ₂ O ₃	Fe ₂ O ₃	MgO	SO ₃	K ₂ O	Na ₂ O	TiO ₂	P ₂ O ₃	Loss on Ignition
a)	19.5	63.2	4.8	3.5	1.5	2.7	0.6	0.1	–	–	4.1
b)	19.1	65.1	4.9	2.9	1.1	3.0	0.5	0.2	0.1	0.1	2.5

2.1.2. Sand

The sand used here is a French normalized sand made by Société Nouvelle du Littoral in accordance with the EN 196-1 standard [30]. It is composed of natural quartz sand (silica content 99%). The sand grains are uncrushed and of rounded shape.

2.1.3. Ferronickel slag

The ferronickel slags were provided by Société Le Nickel- ERAMET (SLN) in New Caledonia). The average particle size of the granulated slag is about 4 mm. The raw FNS grains are ground to powders ($<63 \mu\text{m}$) using high energy ball milling for 30 min. The specific gravity of the slag is 2.92 g cm^{-3} and the Blaine fineness is $6700 \text{ cm}^2 \text{ g}^{-1}$.

2.1.4. *Crepidula fornicata* shells

The *Crepidula fornicata* shells were collected from a fish company in Normandy (France) first ground and screened on site. The raw *Crepidula fornicata* shell grains are secondly ground at ESITC laboratory to powder ($<63 \mu\text{m}$) using high energy ball milling for 30 min. The obtained powder is dried in an oven at $120 \text{ }^\circ\text{C}$ for 24 h in order to remove remaining organic traces. The specific gravity of the *Crepidula fornicata* shells is 2.73 g cm^{-3} and the Blaine fineness is $8140 \text{ cm}^2 \text{ g}^{-1}$.

2.1.5. Mortars mix design

All studied mortars are elaborated with a water on cement ratio (W/C) fixed to 0.5 and a sand to cement ratio at 3, according to EN 196-1 [30]. After mixing, the mortars were filled into square prism molds ($40 \times 40 \times 160 \text{ mm}$). The molds were subjected to 60 hits on a vibrating table after pouring of each layer to expel the air. The molds were then placed in a special confined room temperature ($20 \pm 1 \text{ }^\circ\text{C}$ and relative humidity of 90%). The mortar specimens were demolded 24 h after manufacturing and then conserved at controlled at room conditions until the time of testing. Nine mortar mixtures were elaborated in this study (Table 2). The cement has been replaced by FNS at 0%, 10%, 15% and 30 wt.%. In addition, the cement has also been replaced by a mixture with equal proportions of FNS and CR in the range of 10%, 20%, 30%, 40% and 60 wt.%.

2.2. Characterization techniques

Elemental analyses by Energy Dispersive X-Ray spectroscopy (EDS) were performed using a SUPRA™ 55 (SAPPHIRE; Carl Zeiss, Jena,

Table 2

Composition of the different mortar mixes.

Sample	Mass substitution of cement by FNS (wt.%)	Mass substitution of cement by <i>Crepidula</i> (wt.%)
CM	0	0
FNS10	10	0
FNS15	15	0
FNS30	30	0
FNS5-CR5	5	5
FNS10-CR10	10	10
FNS15-CR15	15	15
FNS20-CR20	20	20
FNS30-CR30	30	30

Germany). The samples were carbon coated and images were recorded using an acceleration voltage of 20 kV.

The analyses of FNS composition were performed by SARM/CRPG laboratory, Nancy (France). Major elements were analyzed by ICP-OES, while trace elements (As–Zr) were analyzed by ICP-MS. Sulphur and CO₂ by infrared absorptiometry, and FeO by volumetry (see SARM-CRPG website for further information about detailed methods, detection limits and precision).

X-ray fluorescence analyses were acquired using an Inel Equinox 3500 spectrometer, equipped with a Cu microfocus source, parabolic multilayer mirror on the primary beam, and an Amptek X-123SDD Silicon Drift Detector placed vertically 10 mm over the sample to ensure high sensitivity even with low-atomic number elements.

X-ray powder diffraction data were performed at room temperature using a Panalytical X'pert Pro diffractometer (two-circle diffractometer, θ - 2θ Bragg-Brentano mode) using the monochromatized Cu-K α average radiation ($\lambda_{\alpha 1} = 1.7890 \text{ \AA}$, $\lambda_{\alpha 2} = 1.7929 \text{ \AA}$). Data are collected for 2θ varying from 15° to 100° for 2 sec per 0.01° step (2 h/scan). The NIST SRM-660b LaB₆ standard powder was used to calibrate the instrumental contribution [31]. Phase identification and quantification were performed using the Crystallography Open Database and the Full-Pattern Search-Match procedure [32]. The Rietveld refinement was performed using the MAUD software [33].

All Raman spectra were recorded at room temperature using a Thermo Fisher Scientific DXR Raman microscope (Thermo Fisher Scientific Inc., Waltham, MA, USA) with a 532 nm laser as an excitation source. The Raman spectrometer is equipped with a 900 lines/mm diffraction grating. A 50X long-distance objective was selected to focus the laser beam onto the surface and collect the scattered light in a backscattering geometry. Data was collected over a range of 50–2200 cm⁻¹. The spectral regions from 3200 to 4000 cm⁻¹ were investigated for the C–S–H species and ettringite, in order to reveal the OH⁻ and the H₂O stretching mode region. The spot diameter of the laser was estimated to 0.8 μm and the spectral resolution to 3 cm⁻¹. Raman spectra were systematically recorded twice at low laser power (2 mW) and with an integration time of 120 s. We used the Origin software and Gaussian curves as elementary fitting functions. The mineral compositions were determined by comparing the collected Raman spectra to those reported in the Raman Open Database ROD [34].

2.3. Test methods

2.3.1. Specific surface area

The specific surface area of each cement mixture used in this study was determined with the Blaine air permeability apparatus according to the ASTM C-204 test method [35].

2.3.2. Fresh properties of mortars

Workability tests were carried out on fresh mortar according to the NF P18-452 standard [36]. The testing device consists of a compartment divided in two unequal volumes by a removable wall. The test measures the time taken for the mortar to flow from the large compartment to the smaller one under the influence of the imposed vibration.

The initial and final setting times were also measured for all mortar mixtures. These tests consist in measuring the time necessary for a plunger assembly with total weight of 1000 g to penetrate into the material. The initial setting time is effective when the distance between the end of plunger and the base-plate is 2.5 mm according to the NF P 15-431 standard [37].

2.3.3. Mechanical properties of hardened mortars

Mechanical properties of the mortars were measured using compressive and three-point bending tests in accordance with the EN 196-1 standard [30], on all samples from 2 days to 28 days of curing. The compression tests were performed at a loading rate of 40 N min⁻¹ while 3-points bending tests were displacement-controlled at a rate of 0.07

mm min⁻¹.

3. Results and discussion

3.1. Microstructural characterization of FNS

The mineralogical and chemical properties of the FNS are important parameters, which influence their recycling. Table 3 shows the bulk chemical analyses of FNS powder.

The slag sample is mainly composed of about 52 wt% of SiO₂, 32 wt.% of MgO and 12.6 wt.% of total iron reported as Fe₂O₃. The majority is divalent iron (FeO: 11.3 wt.%). Minor compounds are, 2.3 wt.% Al₂O₃, about 0.5 wt.% of Na₂O and MnO, 0.3 wt.% of CaO and 0.4 wt.% total H₂O. CO₂ is low (0.16 wt.%). Other minor compounds (K₂O and TiO₂) are below 0.04 wt.%.

Among the trace elements, of about 7900 ppm of Cr, 670 ppm of Ni, 260 ppm of Zn, 65 ppm of V, 61 ppm of Co, and 20 ppm of Sc are the highest values. Very low values of As, Cd, U and Th are reported (Table 3).

A XRD pattern of the FNS sample can reasonably be refined using 4 main phases (Fig. 1 and Table 4). Quantitative phase analysis using Rietveld refinement indicates quartz and forsterite as the two major phases.

With agreement factors of $R_{wp} = 3.9\%$ and $R_B = 2.5\%$, and a Goodness of Fit below 2 (GoF = 1.76), the fit ensures quantitative estimates of the phases and their structural-microstructural characteristic. The analysis of the FNS diffraction diagram indicates that quartz is the dominant phase (50.9%), followed in a decreasing order by Ni-bearing forsterite (Ni,Mg)₂SiO₄ (29.4%), silica (13.5%) and enstatite (3.2%). These phases were identified in each slag powder batch independently of their particle sizes.

Raman analyses confirm that FNS is a mainly crystalline heterogeneous material whose main components are forsterite (Mg,Ni)₂SiO₄, quartz, silica and enstatite (Mg,Fe)₂SiO₃ with traces of chromite (FeCr₂O₄), calcite (CaCO₃) and akaganeite (β -FeO_{1-2x}(OH)_{1+x}Cl_x) (Figs. 2 and 3). Quartz is formed in silica-rich scories during cooling and solidification. Forsterite shows high thermal stability with a melting point of 1890 °C [38,39]. It is known that forsterite occurs at low temperature after reaction between MgO and silica [38]. In an excess of quartz and silica, forsterite reacts with SiO₂ to form enstatite (Mg₂Si₂O₆) [40].

3.1.1. Phases detected by XRD and Raman spectroscopy

The Raman spectrum of the silica structure is shown in Fig. 2a. The refinement was possible with 6 Gaussians (Table 5). The structure of the vitreous-like silicate network is mainly determined by the degree of the silicate tetrahedra polymerization. It is described by the abundance of different Q_n species, where Q_n refers to a tetrahedron linked by bridging oxygen atoms to n (0–4) adjacent tetrahedra. Q₀ corresponds to an isolated monomer, Q₁ and Q₂ to chains, and Q₃ and Q₄ reflect the interconnected structures.

The Raman spectrum of silica present in FNS, is composed of broad peaks. In the Q_n region, the vibration modes of the Q₁, Q₂ and Q₃ species are centred at 880, 940 and 1010 cm⁻¹, respectively. The band at 595 cm⁻¹ is attributed to the twisting and stretching vibration modes of the Si–O–Si bonds [41–43]. The vibration mode at 675 cm⁻¹ is attributed to a poorly crystalline calcium-magnesium silicate [44,45]. The band at 750 cm⁻¹ is assigned to the Si–O stretching vibration with a dominant Si motion [46]. The ratio Q₃/Q₂ is high, indicating an enhancement in the number of Q₃ silicon sites compared to Q₂ and Q₁ and a high degree of polymerization. In general, a higher degree of polymerization in vitreous-like structures leads to higher compressive strengths [47,48].

For forsterite (Fig. 2b), the bands in the 800 and 1100 cm⁻¹ range are attributed to SiO₄ internal stretching vibrational modes [48]. The features observed in that region are a doublet with peaks at 818 and 848 cm⁻¹ whose relative intensities are function of the crystal orientation.

Table 3

Elemental composition of FNS (wt.%) obtained from ICP-MS and ICP-OES measurements on ground FNS powders, normalized to most stable oxides. d.l.: detection limit.

Oxide	(wt.%)	Element	$\mu\text{g/g}$	Element	$\mu\text{g/g}$	Element	$\mu\text{g/g}$	Element	$\mu\text{g/g}$
SiO ₂	51.67	As	d.l	Hf	0.22	Ta	0.06	Nd	1.48
Al ₂ O ₃	2.29	Ba	16.24	In	d.l	Th	0.44	Sm	0.34
Fe ₂ O ₃ (FeO)	12.58 (11.3)	Be	0.24	Mo	2.15	U	0.16	Eu	0.08
MnO	0.46	Bi	d.l	Nb	0.38	V	65	Gd	0.36
MgO	31.56	Cd	d.l	Ni	665	W	d.l	Tb	0.06
CaO	0.31	Co	61	Pb	1.34	Y	3.31	Dy	0.41
Na ₂ O	0.50	Cr	7932	Rb	1.41	Zn	236	Ho	0.09
K ₂ O	0.03	Cs	0.17	Sb	0.22	Zr	8.37	Er	0.27
TiO ₂	0.04	Cu	9.19	Sc	24	La	1.53	Tm	0.05
P ₂ O ₅	d.l	Ga	0.63	Sn	0.45	Ce	2.49	Yb	0.29
Total	99.44	Ge	0.16	Sr	13	Pr	0.37	Lu	0.05

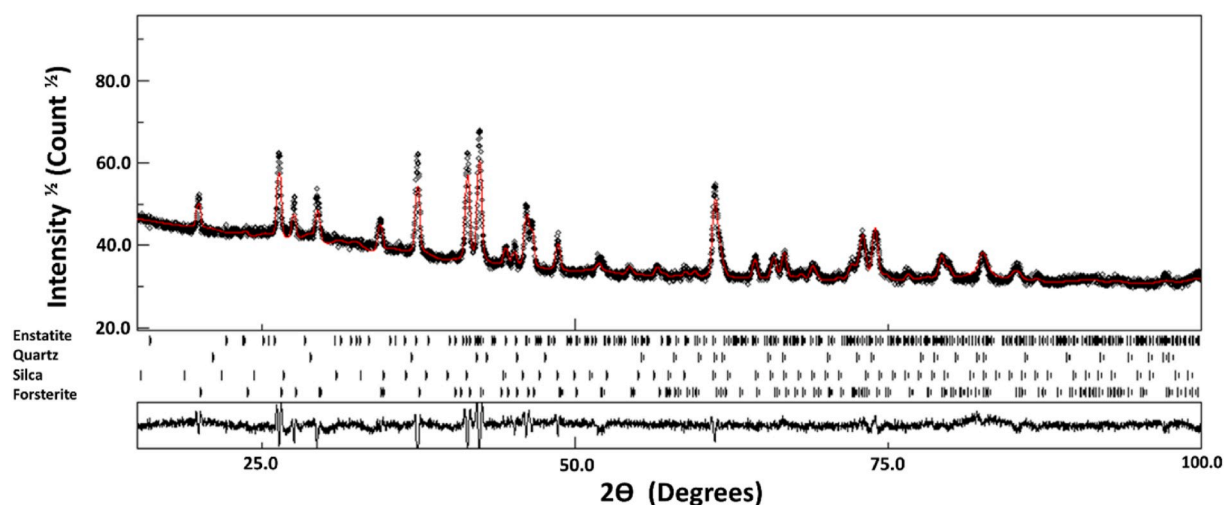


Fig. 1. X-ray diffraction pattern of FNS powder refined using the MAUD software. The calculated pattern (red line) is superimposed to the observed profile (dotted line). The difference curve ($I_{\text{obs}} - I_{\text{calc}}$) is shown at the bottom. (For interpretation of the references to colour in this figure legend, the reader is referred to the Web version of this article.)

Table 4

Refined values of lattice parameters, unit cell volume, average crystallite size and microstrain $\langle e^2 \rangle^{1/2}$, model used and the atom occupancies. One standard deviation for the last digit, as obtained from the refinement, is indicated in parenthesis.

Phase Formula	COD reference	V (%)	Lattice type Space group	Lattice parameters (Å)	Isotropic mean crystallite size $\langle D \rangle$ (nm)	Isotropic microstrain $\langle e^2 \rangle^{1/2}$ (r.m.s.)
Forsterite Mg ₂ SiO ₄	9000319	39.5 (4)	Orthorhombic Pbnm	a = 4.751 (1) b = 10.202 (1) c = 5.968 (2)	834 (20)	6 10 ⁻⁴
Enstatite Mg ₂ Si ₂ O ₆	9014117	7.2 (2)	Orthorhombic Pbca	a = 18.595 (1) b = 8.797 (1) c = 5.231 (1)	253 (15)	1 10 ⁻³
Silica SiO ₂	1011097	11.6 (4)	Cubic P213	a = 9.423 (1)	121 (10)	0
Quartz SiO ₂	9000594	41.7 (5)	Trigonal P3 ₂ 21	a = 5.641 (2) c = 5.247 (2)	92 (4)	1 10 ⁻⁴

These vibration bands result from the coupled asymmetric and symmetric vibrations of SiO₄ tetrahedra. The bands in the 400–800 cm⁻¹ range are due to internal bending of the SiO₄ tetrahedra. Bands below 400 cm⁻¹ are due to lattice modes and dominated by rotations of SiO₄ tetrahedra and translations of cations octahedra (magnesium motion) in the crystal lattice [49,50]. Forsterite may play an important role during the partial replacement of cement by slag. Indeed, it is known that magnesium-rich binder can lead to strength development and durability of cementitious materials [51].

The Raman spectrum of quartz (Fig. 2c) shows a strong Raman mode of the α -phase at 462 cm⁻¹, which corresponds to symmetric stretching

of oxygen in the SiO₄ tetrahedra [52]. Raman bands below 300 cm⁻¹ correspond to combined translations and rotations of the SiO₄ tetrahedra and the band present at 805 cm⁻¹ is assigned to the Si–O asymmetric stretching motions within tetrahedral SiO₄ units.

The Raman spectrum of enstatite (Fig. 2d) can be divided into 5 regions [53–56]: (1) bands in the 800–1100 cm⁻¹ range are assigned to Si–O stretching vibrations, related to the non-bridging Si–O bonds; (2) the vibration modes in the range 650–750 cm⁻¹ are assigned to the Si–O stretching modes of the bridging O atoms; (3) the bending O–Si–O modes are present in the 500–600 cm⁻¹ range; (4) two vibration modes may result from the Mg–O octahedron modes (375–500 cm⁻¹) and (5)

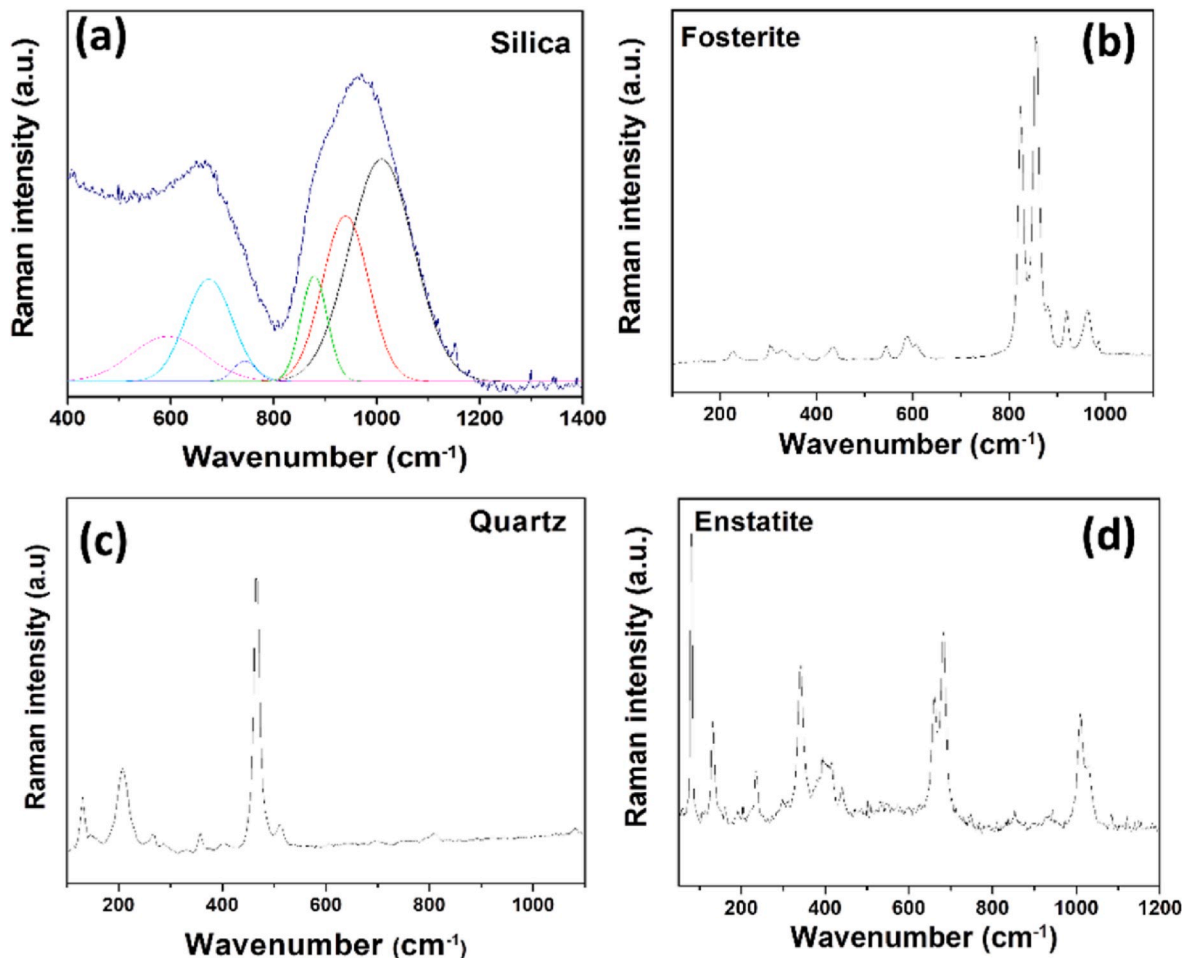


Fig. 2. Raman spectra of: (a) silica, (b) forsterite, (c) quartz and (d) enstatite.

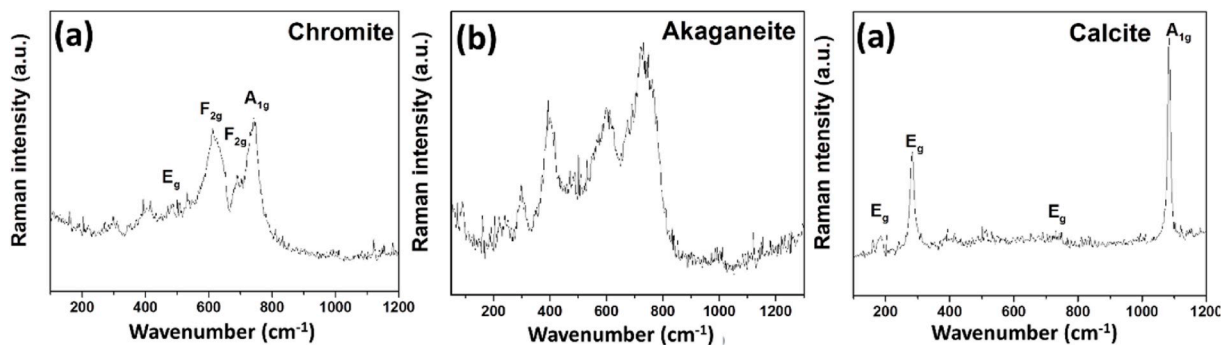


Fig. 3. Raman spectra of (a) chromite, (b) akaganeite and (c) calcite.

Table 5
Refined centers for Gaussian functions for the Raman spectrum of silica.

Peaks	Vibration mode	Center
1	Q ₃	1010
2	Q ₂	940
3	Q ₁	880
4	Si–O stretching	750
5	O–(Ca, Mg, Si)–O bending	675
6	O–(Mg, Si)–O bending	595

the Fe–O octahedron vibration modes (225–350 cm⁻¹).

3.1.2. Phases only detected by Raman spectroscopy

The Raman spectrum of chromite (Fig. 3a) exhibits various bands associated to the Fe–O and Cr–O bond-stretching [57]: a broad and intense band at 780 cm⁻¹ attributed to symmetric stretching A_{1g} (ν₁), two bands at 730 and 485 cm⁻¹ assigned to F_{2g} (ν₄) and E_g (ν₂) modes respectively, and a broad and intense band at 590 cm⁻¹ due to the F_{2g} (ν₃) mode.

Fig. 3b shows the Raman spectrum with the bands around 308, 390, 535 and 720 cm⁻¹, characteristic for akaganeite (β-FeO_{1-2x}(OH)_{1+x}Cl_x) [58]. The Raman features are similar to that reported by El Mendili et al.

[59]. Akaganeite forms in chlorine rich, low pH 3 to 4 environments at temperature about 60 °C, e.g., in hot springs and volcanic deposits [60]. It has a monoclinic crystal structure and always contains Cl^- ions. As shown by Keller [61], akaganeite can contain up to 6 wt.% chloride. It is also preferentially formed compared to goethite and lepidocrocite in environments with high concentration of Fe^{2+} and Cl^- . The presence of akaganeite in FNS may result from the cooling of slag with seawater.

The Raman spectrum of calcite exhibits four Raman bands (156, 282, 712 and 1088 cm^{-1}) at ambient conditions (Fig. 3c) [62]. The strong Raman band at 1088 cm^{-1} is assigned to the A_{1g} mode, the internal E_g mode is observed at 712 cm^{-1} and the external E_g or lattice modes occur at 282 and 156 cm^{-1} .

The use of quartz as SCM has increased in recent years [63]. Indeed, quartz powder may reduce the initial porosity of the mixture and thereby increasing the final strength. In addition, the reactivity of quartz is very low in an alkaline environment such as the one produced by cement and lime. Quartz, when mixed in certain proportions, improves the properties of both fresh and hard concrete such as durability, permeability and compressive flexural and tensile strengths [63].

The presence of vitreous-like silicates with a high degree of polymerization will lead also to higher compressive strengths. In addition, it is known that magnesium-rich binder can lead to strength development and durability of cementitious materials.

All these results show the potential of FNS addition to produce mortars with high performances.

3.2. Microstructural characterization of CR shell

Table 6 shows the chemical compositions of bulk CR pressed powder determined by EDS analyses. The major element is calcium with traces of Na, Si, S, Mg and Al (<0.6 wt.%). Locally, Mg and Al enrichments were observed (2% and 1%, respectively).

Different Raman spectra for the CR powder were collected from several areas. All areas examined produced the same spectrum with the same vibration modes (Fig. 4), typical of aragonite, the orthorhombic carbonate phase. The Raman lines located at low-wavenumber range (113, 151, 181, 208, 250 and 263 cm^{-1}) are assigned to external optical or lattice modes and result from the interactions between CO_3^{2-} ions and Ca^{2+} . The large-wavenumber vibrational modes ν_4 at 701 and 710 cm^{-1} , ν_2 at 856 cm^{-1} , ν_1 at 1086 cm^{-1} and ν_3 at 1461 cm^{-1} are assigned to the internal modes of the CO_3^{2-} group [64]. These Raman analyses agree with previous XRD determinations [65].

3.3. Mortar mixture properties

3.3.1. Specific surface area

The FNS addition significantly increases the specific surface area (SSA) of the slag-cement powder (Fig. 5). This behavior is due to a larger

Table 6

Elemental composition of CR (wt.%) obtained from SEM-EDS measurements on ground CR powders. *Oxygen and Carbon analyzed by EDS are taken with caution due to low precision; d.l.: detection limit.

Element	(wt.%)
O	36.65* ± 3.4
C	7.44* ± 0.8
Ca	53.72 ± 1.4
Na	0.59 ± 0.06
S	0.45 ± 0.04
Mg	0.53 ± 0.05
Si	0.35 ± 0.04
Al	0.28 ± 0.04
Cl	d.l
Total	100,00

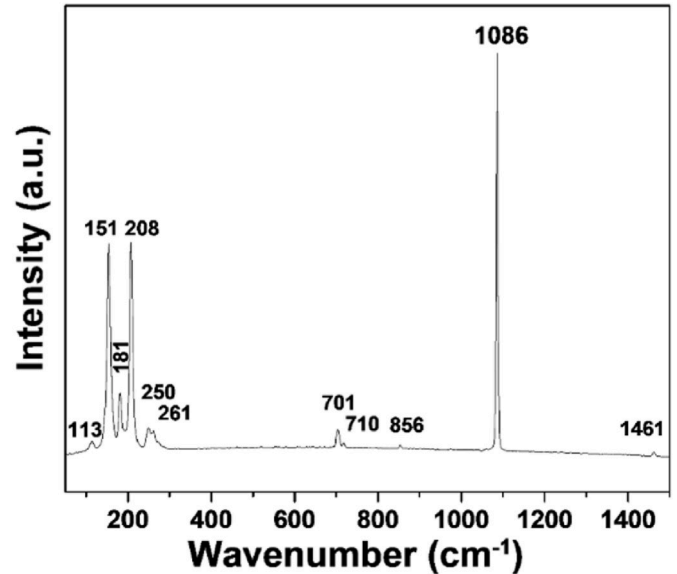


Fig. 4. Raman spectrum of the CR shell.

Blaine specific surface of FNS compared to that of cement (6700 cm^2/g for FNS and 4100 cm^2/g for cement). However, this SSA increase is not a simple linear combination (Fig. 5, line) of the 2 constituting SSA's. It indicates the occurrence of some blockage of the initial specific surface of FNS by mixing with cement. This blockage is clearly visible for FNS10 and is probably due to less FNS particle contact during mixing at this low substitution level.

The FNS and CR shells addition significantly increases the SSA of the slag-cement powder (Fig. 6), for the same reason as previously (Blaine specific surface are 6700 cm^2/g for FNS, 8140 cm^2/g for CR shells and 4100 cm^2/g for cement). With this new mixture, the obtained SSA increase is a simple linear combination (Fig. 6, line).

3.3.2. Density of mortars

Density measurements were performed after 2 and 28 days (Fig. 7). For all mixes, an increase in the bulk density with curing time up to 28 days is observed. Increasing the cement substitution decreases mortar's density at all curing times compared to the control mortar. Since the

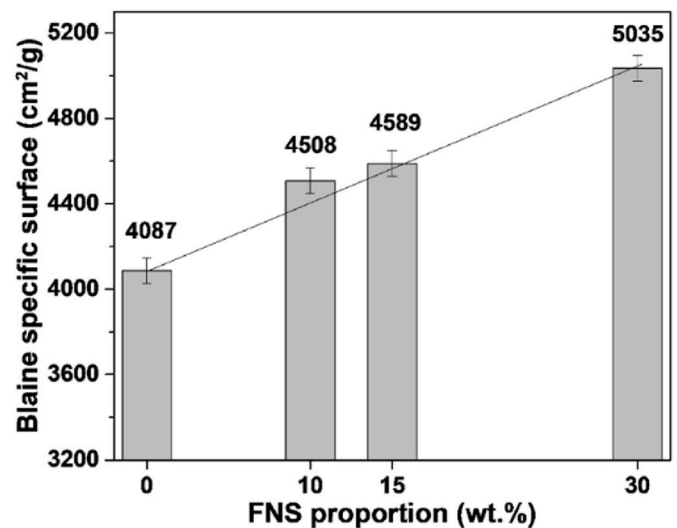


Fig. 5. Evolution of the Blaine specific surface area (SSA) of the cements elaborated with a proportion of FNS in conventional cement. Error bars are standard deviation calculated for 3 replicates.

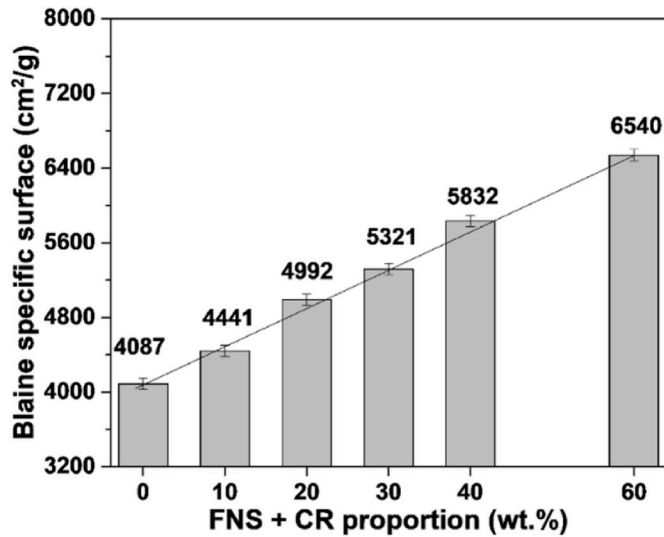


Fig. 6. Evolution of the Blaine specific surface area (SSA) of the cements elaborated with a porportion of FNS and CR in conventional cement. Error bars are standard deviation calculated for 3 replicates.

densities of slag and CR shells are slightly lower than that of the ordinary cement, such an overall density decrease with FNS and CR shells incorporation is expected. However, the density decrease is more pronounced after 2 days than after 28 days. This reflects a further densification with time and porosity decreases.

3.3.3. Workability and setting time of fresh mortars

Flowability experiments show that slag incorporation has no effect on the flow times for all FNS-cement compositions. Indeed, all samples present a flow time with values between 6 and 7 s. For the mixes containing both FNS and CR, up to 30%, the flow time values vary between 6 and 8 s. However, for the larger contents, i.e. 40% and 60%, this flow time becomes larger than 10 s.

Fig. 8 shows the setting time evolution with FNS and FNS-CR contents. For CEM I 52.5, the minimum allowed initial setting time should be above 60 min. The initial and final setting times of all mortar mixtures are within the limits required for the targeted cement class.

Compared to the control sample, samples with only FNS addition (Fig. 8a) exhibit gradual increase in initial and final setting times. While these times decrease by typically 4% at 10% of FNS addition, it increases up to 9% at 15% FNS addition. Finally setting times become larger than for the control sample at larger FNS contents. The introduction of up to

15% FNS accelerates the initial setting. At 30% FNS addition, the initial and final setting times are extended by 2 and 14 min respectively compared to that of the control mix. The setting times below 30% of FNS addition are not modified significantly, and stay for all samples within the NF P 15-431 standard requirements [37]. It confirms the results obtained by the normal consistency tests.

For FNS and CR mixed with mortar (Fig. 8b), the final setting times are increased compared to the control paste. The final setting time of the control paste occurred at 320 min, while substitution of 10 and 60% of mortar by FNS-CR enhanced this value to 325 and 395 min, respectively. The delay in setting time is known to be due to the presence of high amounts of calcium provided by CR. Thus, the final setting time is increased at a high percentage of cement substitution by the high calcium-containing CR shells. The setting time increases almost constantly with FNS-CR incorporation despite the variations observed for the initial setting time.

Using FNS alone, no or insignificant setting time increase is observed.

Taking into account the fixed environmental condition and the use of the same cement, it can be suggested that the decrease of initial setting times is related to low calcium-containing FNS, which reduces the hydration rate at early age.

The increase of the FNS content in the cement increases the separation distance between hydrated cement particles, thus decreases the formation of capillary bridges and delaying then the formation of interlocking network between the particles [66].

3.3.4. Compressive and flexural strength of mortars

The average compressive strengths of mortars after 2, 7, 14 and 28 curing days (Fig. 9) increases with the age of the mortar mixes for all formulations.

Above 10% of FNS substitution (FNS10), the compressive strength decreases (Fig. 9a). The maximum compressive strength values at 2 and 7 days of curing are observed for FNS10. FNS at low contents seems to act more at a young age than in the long term. Indeed, the compressive strength for FNS10 is larger than that of CM, by 5% at 7 days. Below 10% of FNS addition, an increase in non-evaporable water occurs at an early age due to the filler effect, and at a later curing stage due to slag hydration. For higher FNS contents, the filler effect cannot compensate for the dilution effect caused by the large incorporation of slow reacting slag particles [67]. FNS10 acts as a nucleating agent with higher compressive strength at early curing ages. This is due to the formation of additional hydrated products such as C-S-H, which results from the reaction between liberated free portlandite and active silica from FNS.

The compression strength values of all FNS mortars after 28 days are larger than 42.5 MPa. This is an acceptable value for use in the

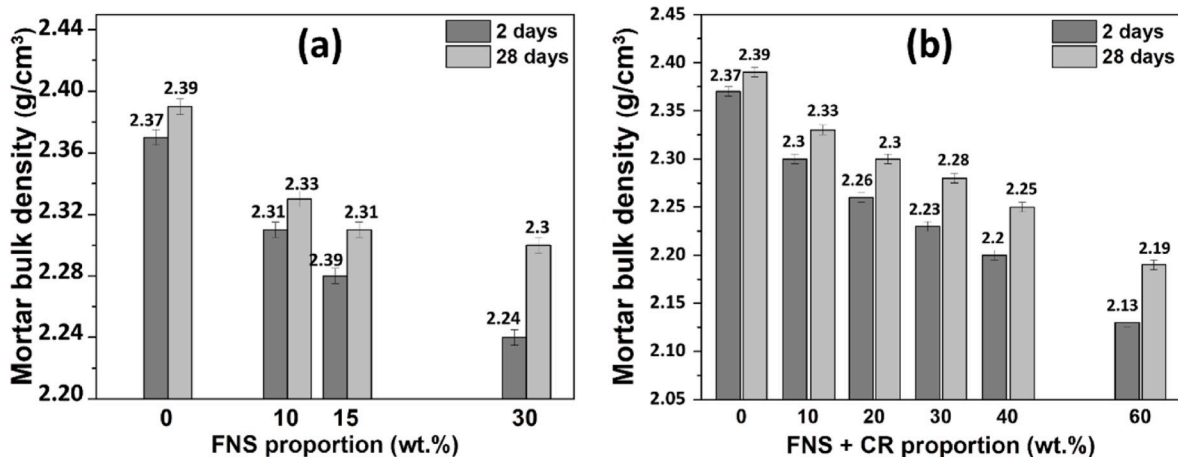


Fig. 7. Variation of the bulk density of the mortars elaborated with different substitution of cement by FNS and CR shells after 2 days and after 28 days of curing.

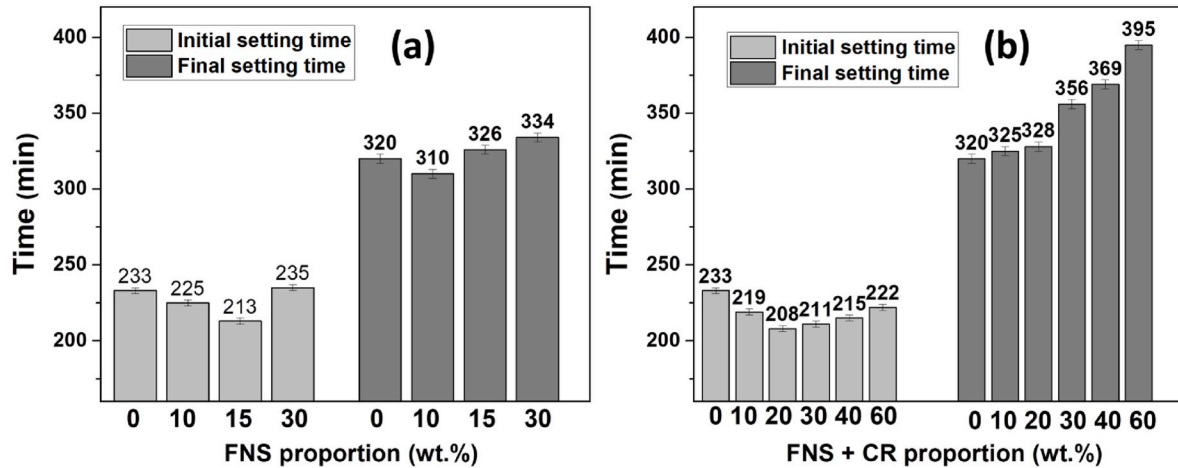


Fig. 8. Initial and final setting time of (a) slag cement and (b) FNS-CR cement.

construction industry as CEM II 42.5.

For FNS-CR mixtures (Fig. 9b), the maximum compressive strength is observed larger than for CM only for the early age of 2 days and for FNS15-CR5. This is due to the microstructural reinforcement and pore or void filling ability by calcium carbonate particles [68]. Thus, CR increases the microstructural density and strength of mortar at this age. For all FNS-CR samples and after 2 days, the compressive strength is always observed lower than for CM. However, the compression strength values of mortars containing up to 20% of FNS-CR remain larger than half the one of CM, still acceptable for application in the construction industry.

The flexural tensile strengths are lower compared to the control mortar for more than 10% of pure FNS addition (Fig. 10a). This is due to the relatively slow pozzolanic reactivity of FNS, due to its richness in SiO_2 [69]. However, as for the compressive strength at early age, the flexural tensile strengths at all curing days of the FNS10 specimen, are slightly larger than that of other mixes including CM. The flexural tensile strengths at 2 and 28 days for FNS10 is larger than the one of CM by 1 and 4%, respectively.

These results are consistent with those obtained for the setting times. The hydration process is accelerated at low FNS incorporation, i.e. up to 10% typically. This leads to an increase in mechanical strength, especially at early age.

The flexural strength and compressive strength of the different FNS-CR mortars exhibit similar behaviours (Figs. 9b and 10b). The hardening kinetics from 2 to 28 days is the same for all specimens. The maximum flexural strength values after 28 days (Fig. 10b) are measured for FNS5-CR5. For 30% of substitution, all flexural strength values appear smaller than half the ones of CM, for a given age. At low substitutions up to 10%, flexural strengths are close to the control mortar for all ages.

In order to achieve higher flexural and compressive strengths, it is recommended to use FNS and FNS-CR powders at low substitution ratio up to 15% and 20%, respectively.

3.3.5. Surface analyses of mortars by Raman spectroscopy

The Raman analyses of the mortar surface of CM after 28 days of curing show the presence of C-S-H and calcite whatever the specimen (Fig. 11), while in the case of FNS5-CR5, in addition to C-S-H and calcite, ettringite is also formed.

The Raman spectra of the C-S-H systems have been widely studied [70,71]. The most intense band at 680 cm^{-1} is attributed to Si-O stretching. The bands present in the low wavenumber range ($100\text{--}360\text{ cm}^{-1}$) are assigned to the lattice vibrations of Ca-O polyhedra, with a contribution at 445 cm^{-1} due to twisting and stretching of Si-O-Si bonds and bands in the $950\text{--}1100\text{ cm}^{-1}$ range associated to symmetric stretching modes of Q_n species in silicates (Si-O). The broad

contribution at high range wavenumbers ($2800\text{--}3600\text{ cm}^{-1}$) is assigned to H_2O stretching modes.

When comparing the Raman spectra of C-S-H formed on non-substituted mortars and on FNS5-CR5, a significant increase of intensity and decrease of bandwidths of the vibrational modes due to the Ca-O polyhedra is observed. This is due to the addition of *Crepidula* shells leading to an increased ordering of the calcium environment, and thus to a higher degree of polymerization. The Raman spectra of the C-S-H shows a decrease of Q_1 (950 cm^{-1}) and an increase of Q_3 (1080 cm^{-1}) for FNS5-CR5 compared to CM. This difference can be interpreted by silica layers cross-linking in the case of FNS5-CR5. In this latter, the C-S-H Raman spectra also shows clearly that the Q_2 species ($1000\text{--}1020\text{ cm}^{-1}$) contribution splits into two main bands at 1006 and 1015 cm^{-1} . This result confirms the modification of the Si-O-Si chain length by a change of the quantity of silica tetrahedra Q_{2p} (pairing) and Q_{2b} (bridging) [72]. This is related to a high quantity of silica provided by FNS. Indeed, the silicates present in FNS react with the excess of calcium hydroxide to form additional C-S-H. Indeed, the large band at 850 cm^{-1} appears in the C-S-H for the FNS5-CR5 sample. This is probably due to the increase of magnesium content.

For ettringite, the Raman spectrum shows an intense peak at 988 cm^{-1} assigned to the $\nu_1(\text{SO}_4)$ mode [62]. In addition, weaker bands are observed at 1113 cm^{-1} , 615 cm^{-1} , 545 cm^{-1} , 450 cm^{-1} and 345 cm^{-1} , attributed to $\nu_3(\text{SO}_4)$, $\nu_4(\text{SO}_4)$, Al-OH stretch, $\nu_2(\text{SO}_4)$ and Al-OH rotation and translation respectively [73]. Two stretching bands are present at large wavenumbers, a sharp one at 3629 cm^{-1} due to OH and a broad one around 3500 cm^{-1} due to water vibrations. Carbonation of the ettringite had occurred, which is evidenced by the presence of the weak band at 1080 cm^{-1} due to C-O stretching in the carbonate groups present in calcium carbonate, attributed to a mixture of calcite and aragonite. This confirms the formation of tricarboaluminate, the carbonate equivalent of ettringite. Carbonate formation is confirmed also by the formation of the C-H vibrations, which appear at 2930 cm^{-1} and 3060 cm^{-1} .

The aragonite (CaCO_3) in the *crepidula* seashell is more than 95% in weight, similarly as in limestone dust that been used in the Portland cement production [25]. In addition, the aragonite crystal structure is a metastable polymorph of CaCO_3 with larger strengths and density than limestone powders [74]. The measured solubility (LogK_{sp}) of aragonite in water at $25\text{ }^\circ\text{C}$ is -8.34 ± 0.02 , leading to the formation of Ca^{2+} and CO_3^{2-} ions in cement formation conditions [75]. The dissolved CO_3^{2-} ions can participate to the hydration reactions, in particular those of the aluminate phases and thus lead to the formation of carboaluminates as opposed to sulfoaluminates, which stabilize the ettringite produced at early ages [76,77]. These carboaluminates are both more voluminous and potentially stiffer [77–79] than the sulfoaluminates, leading to

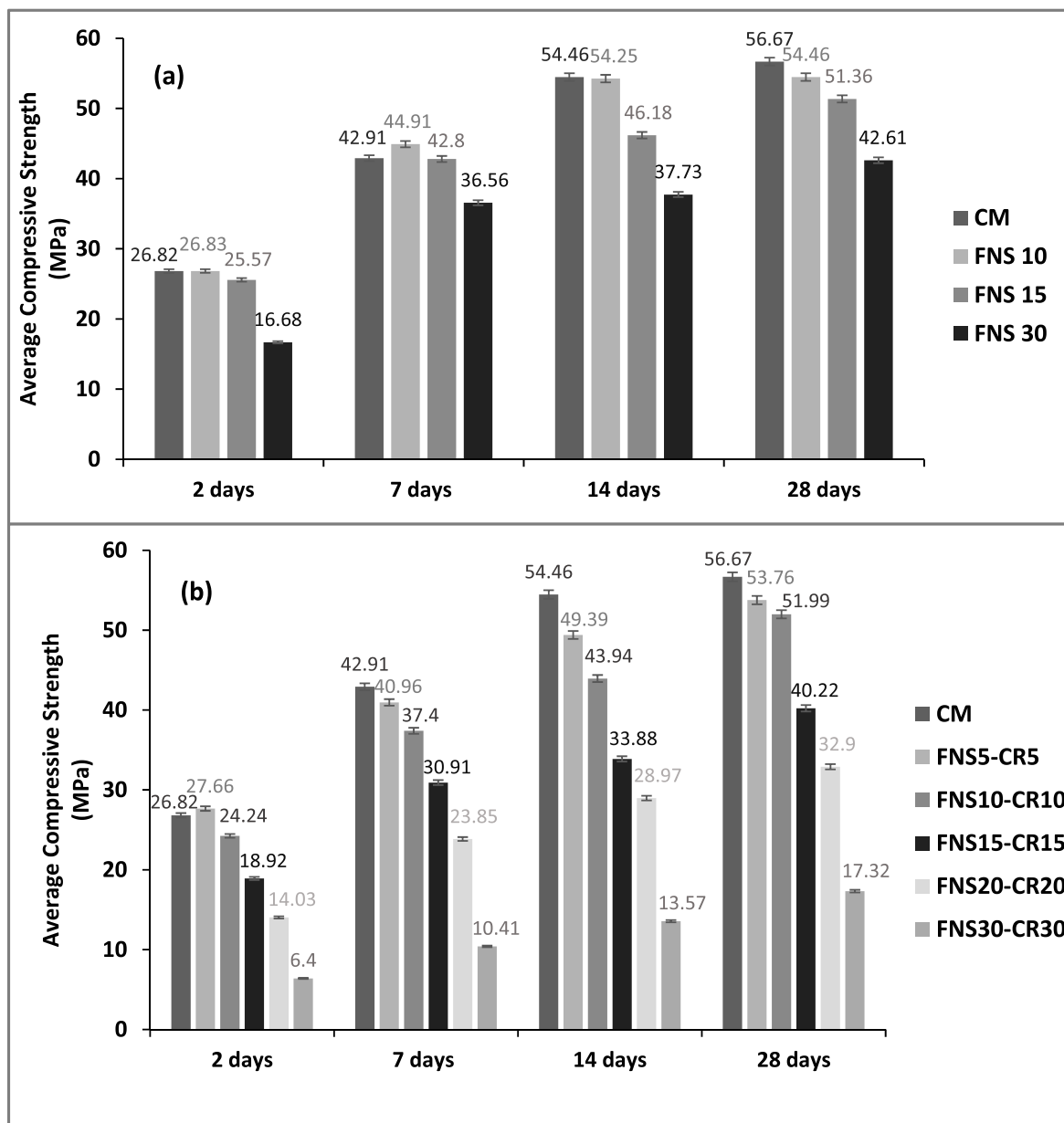


Fig. 9. Average compressive strength at different ages of the mixtures with: (a) FNS and (b) FNS-CR additions.

further reductions of systems porosity and increasing the strengths.

A very limited number of studies are available on the use of FNS as SCM unlike fly ash or blast furnace slag. The here studied FNS originate from nickel laterite ore processing. In particular, saprolite at the base of the laterite profile with low iron oxide (total iron), high magnesium oxides and about 2 wt.% of Al_2O_3 are processed. This is of advantage, as the presence of high proportion of magnesium oxides and Al_2O_3 in cements (binder) reduces shrinkage-cracking in concrete. This magnesium-rich cement can lead to an autogenous expansion at early curing times and can compensate the contraction of the concrete due to cold weather and shrinkage [80]. In addition, X-ray diffraction and Raman analysis showed that magnesium and oxygen are incorporated in FNS slags as crystalline forsterite and enstatite (Figs. 1 and 2). The crystalline structures of enstatite and forsterite are chemically inert and stable [81] and consequently do not participate in hydration reaction to produce expansive e.g. $Mg(OH)_2$ [82,83]. Katsiotis et al. [84] concluded that the presence of FNS slowed down the hydration process in FNS blended concretes. In addition, the authors reported an increase of

compressive strength at later curing stages due to pozzolanic reaction effects of FNS. The consumption of portlandite by the pozzolanic reaction of FNS is considered as the first reason for the reduction of expansion. The use of quartz as a pozzolanic material has increased in recent years [74]. Indeed, pozzolanic materials are generally able to react with the hydrated calcium hydroxide forming the hydrated calcium silicate (C-S-H), responsible for the strength of hydrated cement pastes. Quartz, when mixed in certain proportions, improves the properties of both fresh and hard concrete such as durability, permeability and compressive, flexural and tensile strengths [74,75]. The vitreous-like silica also present in the FNS has a high degree of polymerization. This finding is important for using this material as a cement additive as the above described structure implies a higher degree of stiffness, strength and density of the silicate over time. The silica present in FNS reacted at the later ages and formed secondary calcium silicate hydrate (C-S-H) gel and improved the density of silicate microstructure [85]. In general, a higher degree of polymerization in the vitreous structures leads to higher compressive strength [20,86].

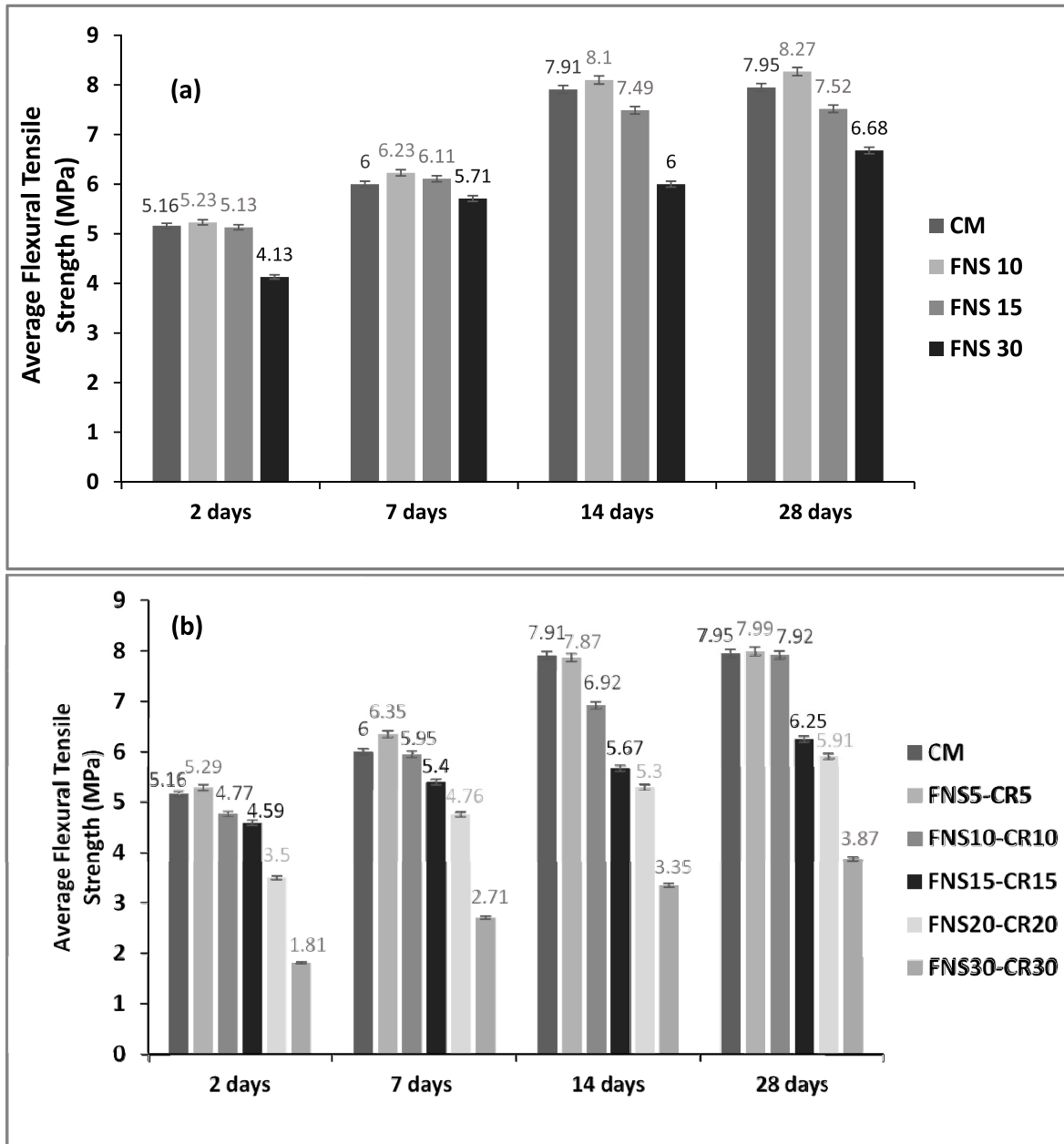


Fig. 10. Average flexural tensile strength at different ages of the mixtures with: (a) FNS and (b) FNS-CR additions.

4. Conclusions

Partial replacement of cement by a FNS-CR mix has been carried out and its effect on the mechanical properties of mortar investigated. The following main conclusions are drawn:

- The partial replacement of cement by up to 30% of FNS-CR mix has no significant effect on the workability of the cement in the fresh state. However, above 30% of incorporation, a slight loss of workability is observed. Water absorption by these additives exhibiting high specific surface area is responsible for this loss of workability.
- With the increase of the FNS-CR mix content, it is globally observed a decrease of the compressive and flexural strengths. Introduction of these less dense additives, compared to cement, limits their use at controlled rates, except for seeking lighter mortars. However, with a rate of up to 20%, the mechanical strengths remain close to those of the control mortar. At 2 days, the addition of FNS-CR at 10% has

positive effect on mechanical performance. This could be directly related to the cement setting acceleration observed for this concentration.

- The greater effectiveness of FNS is attributed to its higher silica content, which leads to the formation of a higher polymerization degree of the silica chains in the C-S-H structure.
- The greater effectiveness of *Crepidula fornicata* shells is attributed to the CO₃²⁻ ions release, leading to the formation of carboaluminates, then to further porosity reduction that increases the strengths.
- A real potential for the use of these by-products as partial replacement of cement, at an optimum rate of 20% is evidenced.

Declaration of competing interest

The authors declare that they have no known competing financial interests or personal relationships that could have appeared to influence the work reported in this paper.

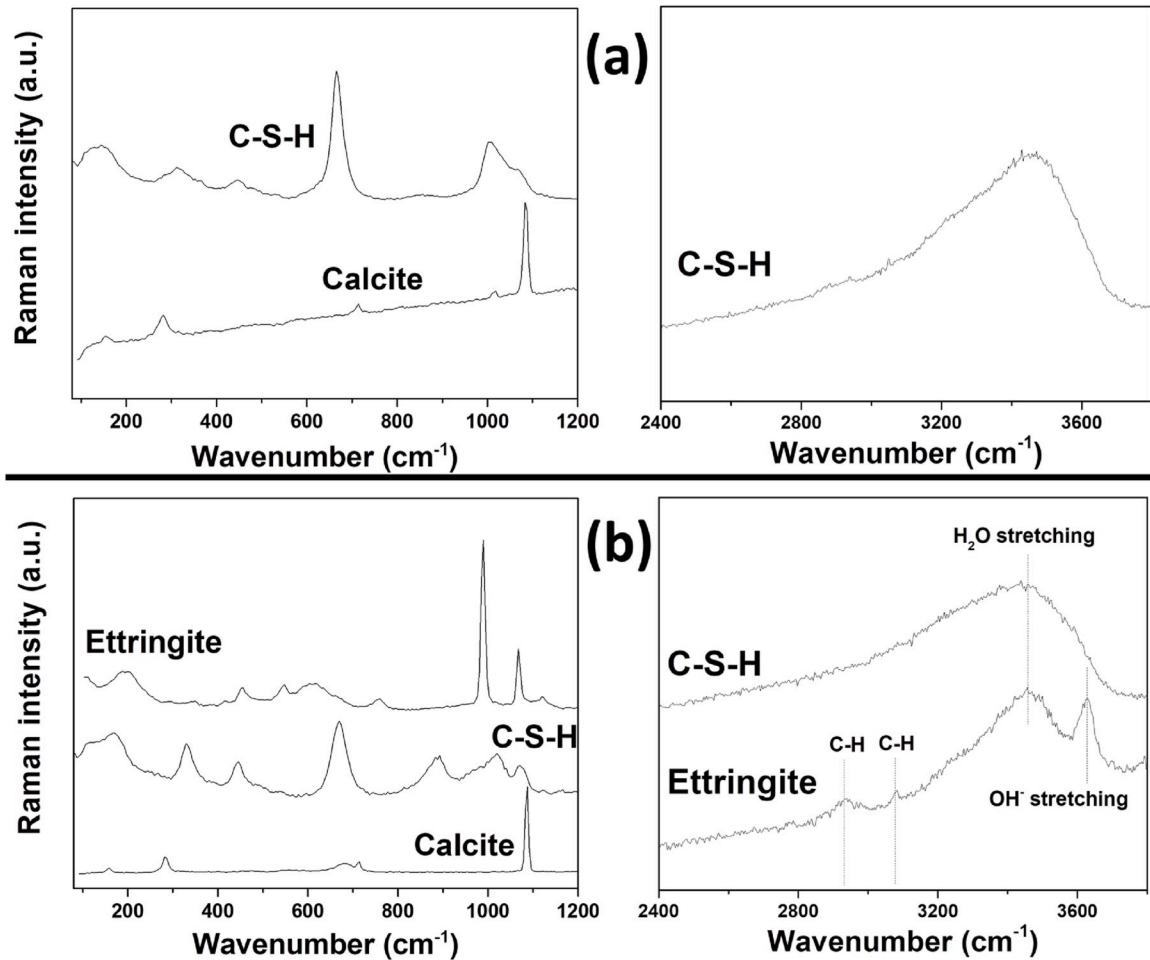


Fig. 11. Raman spectra of the mortar surfaces after 28 days of curing: (a) CM, (b) FNS5-CR5.

CRedit authorship contribution statement

Manal Bouasria: Methodology, Formal analysis, Data curation, Writing - review & editing, Writing - original draft. **Fouzia Khadraoui:** Methodology, Formal analysis, Data curation, Writing - review & editing, Writing - original draft. **Mohammed-Hichem Benzaama:** Validation, Investigation. **Karim Touati:** Validation, Investigation. **Daniel Chateigner:** Validation, Formal analysis, Writing - original draft, Visualization. **Stéphanie Gascoin:** Investigation, Formal analysis. **Valérie Pralong:** Investigation. **Beate Orberger:** Validation, Formal analysis, Investigation, Data curation, Writing - original draft, Visualization. **Laidi Babouri:** Validation, Investigation. **Yassine El Mendili:** Conceptualization, Methodology, Formal analysis, Data curation, Writing - review & editing, Writing - original draft.

Acknowledgements

We thank the SLN-ERAMET for providing the ferro-nickel slags.

Appendix A. Supplementary data

Supplementary data to this article can be found online at <https://doi.org/10.1016/j.job.2020.101587>.

References

- [1] R.M. Andrew, Global CO₂ emissions from cement production, *Earth Syst. Sci. Data* 10 (2018) 195–217.
- [2] J.J. Biernacki, et al., Cements in the 21st century: challenges, perspectives, and opportunities, *J. Am. Ceram. Soc.* 100 (2017) 2746–2773.
- [3] The European Cement Association (CEMBUREAU), Activity Report, first ed., CEMBUREAU, Brussels, Belgium, 2017, pp. 1–42.
- [4] V.M. Malhotra, Role of supplementary cementing materials in reducing greenhouse gas emissions, in: O.E. Gjørsv, K. Sakai (Eds.), *Concrete Technology for a Sustainable Development in the 21st Century*, E, FN Spon, London, 2000, pp. 226–235.
- [5] S. Siddique, *Waste Materials and By-Products in Concrete*, Springer-Verlag Berlin Heidelberg, 2008, <https://doi.org/10.1007/978-3-540-74294-4>.
- [6] Y. Sakoi, M. Aba, Y. Tsukinaga, S. Nagataki, Properties of concrete using ferro-nickel slag aggregate, in: *Proceedings of the 3rd International Conference on Sustainable Construction Materials and Technologies*, 2013, pp. 1–6. Tokyo, Japan.
- [7] P. Higuera, Évaluation Technico-Économique des Débouchés de Valorisation des Scories de Nickel. Territoire : Nouvelle-Calédonie, IAE Nantes—Économie & Management Université de Nantes: Nantes, France, 2019.
- [8] B.V. Tangahu, I. Warmadewanthi, D. Saptarini, Ferro-nickel slag performance from reclamation area in Pomalaa, Southeast Sulawesi Indonesia, *Adv. Chem. Eng. Sci.* 53 (2015) 408–412.
- [9] Z. Wang, Z. Chen, Hydration mechanism of composite binders containing blast furnace ferro-nickel slag at different curing temperatures, *J. Therm. Anal. Calorim.* 1313 (2018) 2291–2301.
- [10] E. Voutsas, K. Magoulas, G. Andronikos, S. Stamataki, Recycling ferrous-nickel slag in blast cleaning, *Waste Manag. Res.* 20 (2002) 269–278.
- [11] E. Ibrahim, P. Barnabé, E. Ramanaidou, E. Pirarda, Mapping mineral chemistry of a lateritic outcrop in New Caledonia through generalized regression using Sentinel-2 and field reflectance spectra, *Int. J. Appl. Earth Obs. Geoinf.* 73 (2018) 653–665.
- [12] Ashok Dr, Dalvi D., Gordon Bacon W., Robert Mr, Osborne C. The Past and the Future of Nickel Laterites, PDAC 2004 International Convention, Trade Show, Investors Exchange March 7-10, 2004, pp. 18.
- [13] Le Nickel – SLN, FNS: a promising construction material for the Pacific Region. <http://sln.nc/sites/default/files/flippingbook/slnslg/fichiers/assets/common/downloads/publicati622on.pdf>, 2017. (Accessed 7 January 2017).
- [14] Q.D. Nguyen, M. Khan, A. Castel, T. Taehwan Kim, Durability and microstructure properties of low-carbon concrete incorporating ferro-nickel slag sand and fly ash, *J. Mater. Civ. Eng.* 31 (2019), 04019167.

- [15] A. Saha, P.K. Sarker, Sustainable use of ferronickel slag fine aggregate and fly ash in structural concrete: mechanical properties and leaching study, *J. Clean. Prod.* 162 (2017) 438–448.
- [16] E. Anastasiou, K.G. Filikas, M. Stefanidou, Utilization of fine recycled aggregates in concrete with fly ash and steel slag, *Construct. Build. Mater.* 50 (2014) 154–161.
- [17] A.K. Saha, P.K. Sarker, Durability of mortar incorporating ferronickel slag aggregate and supplementary cementitious materials subjected to wet-dry cycles, *Int. J. Concr. Struct. Mater.* 12 (2018) 29.
- [18] M.A. Rahman, P.K. Sarker, F.U.A. Shaikh, A.K. Saha, Soundness and compressive strength of Portland cement blended with ground granulated ferronickel slag, *Construct. Build. Mater.* 140 (2017) 194–202.
- [19] O.M. Olofinnade, A.N. Ede, J.M. Ndambuki, G.O. Bamigboye, Structural properties of concrete containing ground waste clay brick powder as partial substitute for cement, *Mater. Sci. Forum* 866 (2016) 63–67.
- [20] Z. Ma, Q. Tang, D. Yang, G. Ba, Durability studies on the recycled aggregate concrete in China over the past decade: a review, *Adv. Civ. Eng.* 2019 (2019) 1–19.
- [21] France Agri Mer, Les filières pêche et aquaculture en France, 2019.
- [22] L.B. Sickels-Taves, M.S. Sheehan, *The Lost Art of Tabby Redefined: Preserving Oglethorpe's Architectural History*, Architectural Conservation Press, Southfield, 1999.
- [23] B.A. Tayeh, M.W. Hasaniyah, A.M. Zeyad, M.O. Yusuf, Properties of concrete containing recycled seashells as cement partial replacement: a review, *J. Clean. Prod.* 237 (2019) 117723.
- [24] A.S.B.W. Mohammad, N.H. Othman, M.H.W. Ibrahim, M.A. Rahim, S. Shahidan, R. Abd Rahman, A review on seashells ash as partial cement replacement, *IOP Conf. Ser. Mater. Sci. Eng.* 271 (2017), 012059.
- [25] S. Mosher, G.W. Cope, F.X. Weber, D. Shea, T.J. Kwak, Effects of lead on Na⁺, K⁺-ATPase and hemolymph ion concentrations in the freshwater mussel *Elliptio complanata*, *Environ. Toxicol.* 27 (2012) 268–276.
- [26] EN 197-1, Ciment - Partie 1: Composition, spécifications et critères de conformité des ciments courants, 2001.
- [27] H.F.W. Taylor, *Cement Chemistry*, second ed., Thomas Telford, 1997.
- [28] G. Menendez, V.L. Bonavetti, H. Donza, M. Trezza, E.F. Irassar, Ternary blended cement for high-performance concrete. High-performance concrete. Performance and quality of concrete structures, in: *Proceedings, Third International Conference. American Concrete Institute*, 2002. Brazil.
- [29] Z. Tan, G. De Schutter, G. Ye, Y. Gao, The effect of limestone powder addition on strength of slag blended cement, in: *CONSEC13 - Seventh International Conference on Concrete under Severe Conditions-Environment and Loading*, 2013, pp. 23–25 (Nanjing, China).
- [30] NF EN 196-1, Méthodes d'essais des ciments - Partie 1 : détermination des résistances - Méthodes d'essais des ciments, 2016.
- [31] G. Caglioti, A. Paoletti, F.P. Ricci, Choice of collimators for a crystal spectrometer for neutron diffraction, *Nucl. Instrum.* 3 (1958) 223–228.
- [32] S. Grazulis, A. Daškevič, A. Merkys, D. Chateigner, L. Lutterotti, M. Quirós, N. R. Serebryanaya, P. Moeck, R.T. Downs, A. Le Bail, *Crystallography Open Database (COD): an open-access collection of crystal structures and platform for world-wide collaboration*, *Nucleic Acids Res.* 40 (D1) (2012) D420–D427.
- [33] L. Lutterotti, S. Matthies, H.R. Wenk, A.S. Schultz, J.W. Richardson, Combined texture and structure analysis of deformed limestone from time-of-flight neutron diffraction spectra, *J. Appl. Phys.* 81 (1997) 594–600.
- [34] Y. El Mendili, A. Vaitkus, A. Merkys, S. Gražulis, D. Chateigner, F. Mathevet, S. Gascoin, S. Petit, J.-F. Bardeau, M. Zanatta, M. Secchi, G. Mariotto, A. Kumar, M. Cassetta, L. Lutterotti, E. Borovin, B. Orberger, P. Simon, B. Hehlen, M. Le Guen, *Raman Open Database: first interconnected Raman-X-ray diffraction open-access resource for material identification*, *J. Appl. Crystallogr.* 52 (2019) 618–625.
- [35] ASTM C204-18e1, *Standard Test Methods for Finesness of Hydraulic Cement by Air-Permeability Apparatus*, ASTM International, West Conshohocken, PA, 2018.
- [36] NF P18-452, *Concretes - Measuring the Flow Time of Concretes and Mortars Using a Workabilitymeter*, 2017.
- [37] NF P 15-431, P 15-431. Liants hydrauliques - Technique des essais - Détermination du temps de prise sur mortier normal, 1994.
- [38] C. Kosanovic, N. Stubicar, N. Tomašič, V. Beranec, M. Stubičar, Synthesis of a forsterite powder by combined ball milling and thermal treatment, *J. Alloys Compd.* 389 (2005) 306–309.
- [39] M.S.A. Maghsoudlu, T. Ebadzadeh, Z. Sharafi, M. Arabi, Zahabi K.R., Synthesis and sintering of nano-sized forsterite prepared by short mechanochemical activation process, *J. Alloys Compd.* 678 (2016) 290–296.
- [40] R. Michel, M.R. Ammar, P. Simon, E. de Bilbao, J. Poirier, Behaviour of olivine refractories at high temperature: agglomeration in a fluidized bed reactor, *Refractories. Worldforum* 6 (2014) 95–98.
- [41] F.L. Galeener, Planar rings in vitreous silica, *J. Non-Cryst. Sol.* 49 (1982) 53–62.
- [42] D.W. Matson, S.K. Sharma, J.A. Philpotts, The structure of high-silica alkali-silicate glasses. A Raman spectroscopic investigation, *J. Non-Cryst. Sol.* 58 (1983) 323–352.
- [43] P. McMillan, Structural studies of silicate glasses and melts-applications and limitations of Raman spectroscopy, *Am. Mineral.* 69 (1984) 622–644.
- [44] C.-S. Deng, C. Breen, J. Yarwood, S. Habesch, J. Phipps, R. Craster, G. Maitland, Ageing of oilfield cement at high humidity: a combined FEG-ESEM and Raman microscopic investigation, *J. Mat. Chem.* 12 (2002) 3105–3112.
- [45] S. Martinez-Ramirez, M. Frias, C. Domingo, Micro-Raman spectroscopy in white portland cement hydration: long-term study at room temperature, *J. Raman Spectrosc.* 37 (2006) 555–561.
- [46] D.W. Matson, S.K. Sharma, J.A. Philpotts, The structure of high silica alkali silicate glasses. A Raman spectroscopic investigation, *J. Non-Cryst. Solids* 58 (1983) 323–352.
- [47] H. Ma, H. Zhu, C. Yi, J. Fan, H. Chen, X. Xu, T. Wang, Preparation and reaction mechanism characterization of alkali-activated coal gangue-slag materials, *Materials* 12 (2019) 2250.
- [48] Y. El Mendili, D. Chateigner, B. Orberger, S. Gascoin, J.-F. Bardeau, S. Petit, C. Dué, M. Le Guen, H. Pilliere, Combined XRF, XRD, SEM-EDS and Raman analyses on serpentinized harzburgite (Nickel laterite mine, New Caledonia): implications for exploration and geomaterials, *ACS Earth. Space. Chem.* 3 (2019) 2237–2249.
- [49] H. Take, Single crystals by the floating-zone method, *J. Cryst. Growth* 43 (1978) 463–468.
- [50] A. Geiger C.A., A Raman spectroscopic study of Fe-Mg olivines, *Phys. Chem. Miner.* 31 (2004) 142–154.
- [51] A. Chopelas, Single crystal Raman spectra of forsterite, fayalite, and monticellite, *Am. Mineral.* 76 (1991) 1101–1109.
- [52] C.C. Lin, Pressure-induced polymorphism in enstatite (MgSiO₃) at room temperature: clinoenstatite and orthoenstatite, *J. Phys. Chem. Solid.* 65 (2004) 913–921.
- [53] S.K. Sharma, B. Simons, H.S. Yoder Jr., Raman study of anorthite: calcium Tschermak's pyroxene and gehlenite in crystalline and glassy states, *Am. Mineral.* 68 (1983) 1113–1125.
- [54] P. McMillan, Structural studies of silicate glasses and melts: applications and limitations of Raman spectroscopy, *Am. Mineral.* 69 (1984) 633–644.
- [55] P.F. McMillan, A.M. Hofmeister, Infrared and Raman spectroscopy, *Mineralogical Society of America Reviews in Mineralogy* 18 (1988) 99–159.
- [56] V.C. Farmer, Orthosilicate, pyrosilicates, and other finite-chain silicates, in: V. C. Farmer (Ed.), *The Infrared Spectra of Minerals*, Mineralogical Society of London, 1974, pp. 285–303.
- [57] B.J. Reddy, R.L. Frost, Spectroscopic characterization of chromite from the moabaracoa ophiolitic massif, Cuba, *Spectrochim. Acta, Part A* 61 (2005) 1721–1728.
- [58] S. Réguer, P. Dillmann, F. Mirambet, Buried iron archaeological artefacts: corrosion mechanisms related to the presence of Cl-containing phases, *Corrosion Sci.* 49 (2007) 2726–2744.
- [59] Y. El Mendili, A. Abdelouas, A. Ait Chaou, J.-F. Bardeau, M.L. Schlegel, Carbon steel corrosion in clay-rich environment, *Corrosion Sci.* 88 (2014) 56–65.
- [60] A.C. Scheinost, Metal oxides, in: D. Hillel (Ed.), *Book: Encyclopedia of Soils in the Environment*, 2005, pp. 428–438.
- [61] P. Keller, Vorkommen, Entstehung und Phasenwandlung von β -FeOOH in Rost, *Werkstoffe Korrosion* 20 (1969) 102–108.
- [62] A. Ait Chaou, A. Abdelouas, Y. El Mendili, R. Bouakkaz, S. Utsunomiya, C. Martin, X. Bourbon, Vapor hydration of a simulated borosilicate nuclear waste glass in unsaturated conditions at 50°C and 90°C, *RSC Adv.* 5 (2015) 64538–64549.
- [63] A.M. Rashad, S.R. Zeedan, Preliminary study of blended pastes of cement and quartz powder under the effect of elevated temperature, *Construct. Build. Mater.* 29 (2012) 672–681.
- [64] P. Gillet, C. Biellmann, B. Reynard, P. McMillan, Raman spectroscopic studies of carbonates Part I: high-pressure and high-temperature behaviour of calcite, magnesite, dolomite and aragonite, *Phys. Chem. Miner.* 20 (1993) 1–18.
- [65] S. Yalcin, D. Chateigner, L. Le Pluart, S. Gascoin, S. Eve, Investigation of structural and mechanical properties of BioCaCO₃-LDPE composites, *Met. Mater. Int.* 1 (2019) 29–43.
- [66] J. Lizarazo-Marriaga, P.A. Claisse, E. Ganjian, Effect of steel slag and Portland cement in the rate of hydration and strength of blast furnace slag pastes, *J. Mater. Civ. Eng.* 23 (2011) 153–160.
- [67] C.C. Castellano, V.L. Bonavetti, H.A. Donza, E.F. Irassar, The effect of w/b and temperature on the hydration and strength of blastfurnace slag cements, *Construct. Build. Mater.* 111 (2016) 679–688.
- [68] S. Abinaya, S.P. Venkatesh, An effect on oyster shell powder's mechanical properties in self compacting concrete, *Int. J. Innov. Res. Sci. Eng. Technol.* 5 (2016) 11785–11789.
- [69] V.G. Papadakis, S. Antiohos, S. Tsimas, Supplementary cementing materials in concrete. Part II: a fundamental estimation of the efficiency factor, *Cement Concr. Res.* 32 (2002) 1533–1538.
- [70] R.J. Kirkpartick, J.L. Yarger, P.F. McMillan, P. Yu, X. Cong, Raman spectroscopy of C-S-H, tobermorite, and jennite, *Adv. Cement Base Mater.* 5 (1997) 93–99.
- [71] Garbev, P. Stemmermann, L. Black, C. Breen, J. Yarwood, B. Gasharova, Structural features of C-S-H(I) and its carbonation in air-A Raman spectroscopic study. Part I: fresh phases, *J. Am. Ceram. Soc.* 90 (2007) 900–907.
- [72] S. Grangeon, F. Claret, C. Roos, T. Sato, S. Gaboreau, Y. Linard, Structure of nanocrystalline calcium silicate hydrates: insights from X-ray diffraction, synchrotron X-ray absorption and nuclear magnetic resonance, *J. Appl. Crystallogr.* 49 (2016) 771–783.
- [73] S.K. Deb, M.H. Manghnani, K. Ross, R.A. Livingston, P.J.M. Monteiro, Raman scattering and X-ray diffraction study of the thermal decomposition of an ettringite-group crystal, *Phys. Chem. Miner.* 30 (2003) 31.
- [74] N.H. Othman, B.H. Abu Bakar, M.M. Don, M.A.M. Johari, Cackle shell ash replacement for cement and filler in concrete, *Malaysian. J. Civil. Eng.* 25 (2013) 201–211.
- [75] L.N. Plummer, E. Busenberg, The solubilities of calcite, aragonite, and vaterite in CO₂-H₂O solutions between 0 and 90 °C, and an evaluation of the aqueous model for the system CaCO₃-CO₂-H₂O, *Geochim. Cosmochim. Acta.* 46 (1982) 1011–1040.
- [76] T. Matschei, B. Lothenbach, F.P. Glasser, The role of calcium carbonate in cement hydration, *Cement Concr. Res.* 37 (2007) 551–558.
- [77] V.T. Cost, T. Matschei, J. Shannon, I.L. Howard, Extending the Use of Fly Ash and Slag Cement in Concrete Through the Use of Portland-Limestone Cement, in: *2014 International Concrete Sustainability Conference*, Boston, MA, May 12–14, 2014, p. 15.

- [78] K. De Weerd, M. Ben Haha, G. Le Saout, K.O. Kjellsen, H. Justnes, B. Lothenbach, Hydration mechanisms of ternary portland cements containing limestone powder and fly ash, *Cement Concr. Res.* 41 (2011) 279–291.
- [79] J. Moon, J.E. Oh, M. Balonis, F.P. Glasser, S.M. Clark, P.J.M. Monteiro, High pressure study of low compressibility tetracalcium aluminum carbonate hydrates $3\text{CaO} \cdot \text{Al}_2\text{O}_3 \cdot \text{CaCO}_3 \cdot 11\text{H}_2\text{O}$, *Cement Concr. Res.* 42 (2012) 105–110.
- [80] T. Zhang, L.J. Vandeperre, C.R. Cheeseman, Formation of magnesium silicate hydrate (M-S-H) cement pastes using sodium hexametaphosphate, *Cement Concr. Res.* 65 (2014) 8–14.
- [81] C. Klein, C.S. Hurlbut, J.D. Dana, *Manual of Mineralogy*, twenty first ed., Wiley, New Jersey, United States, 1998, pp. 373–375.
- [82] M.S.A. Maghsoudlou, T. Ebadzadeh, Z. Sharafi, M. Arabi, K.R. Zahabi, Synthesis and sintering of nano-sized forsterite prepared by short mechanochemical activation process, *J. Alloys Compd.* 678 (2016) 290–296.
- [83] C. Kosanović, N. Stubičar, N. Tomasić, V. Bermanec, M. Stubičar, Synthesis of a forsterite powder by combined ball milling and thermal treatment, *J. Alloys Compd.* 389 (2005) 306–309.
- [84] N.S. Katsiotis, P.E. Tsakiridis, D. Velissariou, M.S. Katsiotis, S.M. Alhassan, M. Beazi, Utilization of ferronickel slag as additive in Portland cement: a hydration leaching study, *Waste. Biomass. Valoriz.* 6 (2015) 177–189.
- [85] N. Lemonis, P.E. Tsakiridis, et al., Hydration study of ternary blended cements containing ferronickel slag and natural pozzolan, *Construct. Build. Mater.* 81 (2015) 130–139.
- [86] C. Wu, W. Chen, H. Zhang, H. Yu, W. Zhang, N. Jiang, L. Liu, The hydration mechanism and performance of Modified magnesium oxysulfate cement by tartaric acid, *Construct. Build. Mater.* 144 (2017) 516–524.